Journal of Zhejiang University-SCIENCE A (Applied Physics & Engineering)
ISSN 1673-565X (Print); ISSN 1862-1775 (Online)
www.jzus.zju.edu.cn; www.springerlink.com
E-mail: jzus@zju.edu.cn

Analysis of the dynamic stress path under obliquely incident P-waves and its influencing factors*

Bo HUANG[1,2], Qi-qun LI[1,2,3], Dao-sheng LING[†‡1,2], Jing-wen LIU[1,2], Yu WANG[1,2]

([1]*Institute of Geotechnical Engineering, Zhejiang University, Hangzhou 310058, China*)

([2]*MOE Key Laboratory of Soft Soils and Geoenvironmental Engineering, Zhejiang University, Hangzhou 310058, China*)

([3]*CCCC-FHDI Engineering Co., Ltd., Guangzhou 510230, China*)

[†]E-mail: dsling@zju.edu.cn

Received July 6, 2016; Revision accepted Mar. 5, 2017; Crosschecked Sept. 11, 2017

Abstract: The dynamic stress path of a rock and soil mass under seismic action has a crucial influence on its catastrophic behavior. In soil dynamics, earthquakes are commonly simplified as vertically incident shear waves and the seismic stresses in soil are estimated based on rigid foundation models. However, the great effect of P-waves should not be overlooked in strong earthquakes, which have happened frequently in recent years. The characteristics of the dynamic stress path under longitudinal waves with significant oblique incidence are still unclear. Analytical formulas for the seismic stresses at any depth of a semi-infinite elastic space under obliquely incident P-waves are derived, which degenerate into the traditional rigid foundation method in soil dynamics when both the incident angle and Poisson's ratio are taken as zero. Here, we reveal the fundamental characteristics of a dynamic stress path under obliquely incident P-waves. The stress path is proved mathematically to be an oblique ellipse in the plane of normal stress difference and horizontal shear stress. We identify factors affecting the stress path, including the incident angle, Poisson's ratio, and depth corresponding to unit wavelength. The possible variation in the range of an oblique elliptic stress path is systematically analyzed, which lays a theoretical foundation for further study of the dynamic response of sites under obliquely incident seismic waves.

Key words: Near-field earthquakes; P-waves; Oblique incidence; Semi-infinite elastic space; Dynamic stress path
http://dx.doi.org/10.1631/jzus.A1600497 **CLC number:** TU435

1 Introduction

Earthquakes are one of the most serious natural disasters that threaten human survival. Rock and soil mass plays an important role during an earthquake and is not only the intermediary of an earthquake from bedrock to buildings or structures, but also the carrier of disaster. Many studies have indicated that the dynamic stress path of site soil under seismic action has a crucial influence on its catastrophic behavior (Ding, 2010; Gu *et al*., 2012; Li *et al*., 2015). Thus, in the study of earthquakes, particularly near-field earthquakes, the dynamic stress path of site soil is of great significance.

The observation that seismic action causes weakening of contact among soil particles, a subsequent increase in pore pressure, and the development of deformation of soil elements leading to regional disaster, has long been of concern. Due to limited understanding and experimental apparatus, laboratory dynamic testing of the seismic response of soil has been based mainly on the studies of (Seed and Lee, 1966; Thiers and Seed, 1968; Seed and Peacock, 1971; Seed and Idriss, 1971; Seed *et al.*, 1983). Simulations of earthquake loads have considered the effects only of vertically upward propagating shear waves and regarded the foundation as a rigid body (Figs. 1a and 2a).

‡ Corresponding author

* Project supported by the National Natural Science Foundation of China (Nos. 51178427 and 51278451) and the National Basic Research Program (973 Program) of China (No. 2014CB047005)

ORCID: Bo HUANG, http://orcid.org/0000-0002-7293-8618; Dao-sheng LING, http://orcid.org/0000-0002-0604-1175

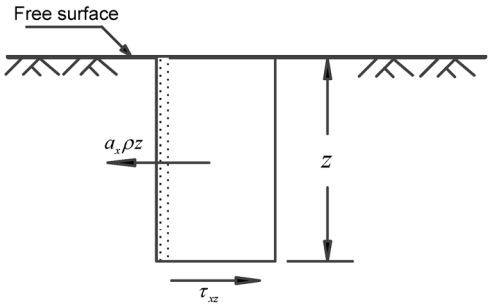

(a)

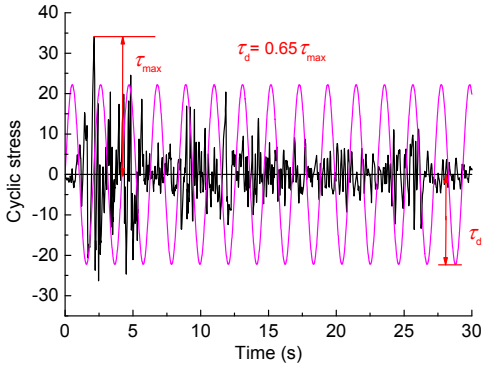

Earthquake magnitude	Number of significant stress cycles, N_c
7	10
7.5	20
8	30

(b)

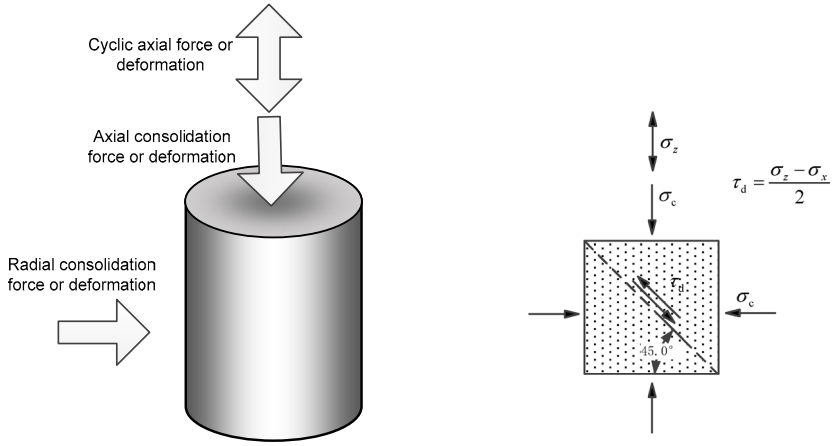

(c)

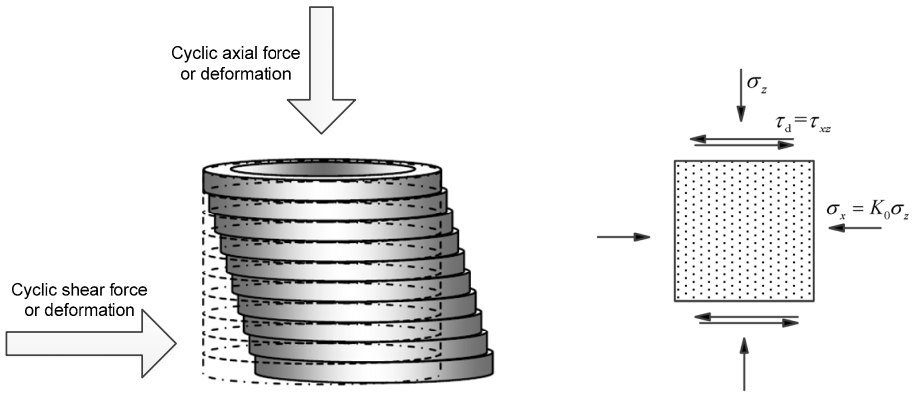

(d)

Fig. 1 Seed and Idriss (1971)'s rigid foundation model and its applications in laboratory tests

(a) Equilibrium of forces near the surface; (b) Actual and equivalent time histories of seismic shear stresses and significant stress cycles in a simplified method; (c) Loaded sample in a dynamic triaxial test; (d) Loaded sample in a dynamic simple shear test. σ_x is the dynamic horizontal normal stress, σ_z is the dynamic vertical normal stress, σ_c is the consolidation stress, τ_d is the dynamic shear stress, K_0 is the coefficient of earth pressure at rest, and τ_{xz} and τ_{zx} are the dynamic horizontal shear stresses, τ_{xz}=τ_{zx}

According to Newton's second law, the relationship among ground surface acceleration, soil density ρ, depth, and the shear stresses generated by S-waves was deduced as

$$\tau_{xz}=\gamma_s z\frac{a_x}{g}, \tag{1}$$

where a_x is the horizontal ground surface acceleration; γ_s is the unit weight of soil; z is the depth of soil unit; g is gravitational acceleration. Irregular seismic shear stresses were simplified as unidirectional exciting sinusoidal waves (Fig. 1b) with a certain number of significant cycles and average equivalent uniform amplitude. The stresses were applied to the soil unit in simple cyclic shear apparatus or dynamic triaxial apparatus, which is still in use today (Figs. 1c and 1d).

Engineers tend to overlook the effect of P-waves for two main reasons: first, P-waves decay rapidly (Gubbins and Snieder, 1991); second, for soil approaching saturation (Poisson's ratio close to 0.5), the difference in horizontal and vertical reciprocating normal stresses (Fig. 2b) induced by vertically incident P-waves is rather small (Ishihara, 1996). This implies that the soil is under cyclic spherical stress and instantaneous changes in pore pressure occur without obvious changes in deformation and strength. However, recent studies showed that if the soil is slightly below saturation, vertical motions induced by vertically incident P-waves can induce a deviator stress of $(\sigma_z-\sigma_x)$ in the soil, rather than a purely compressive stress under the fully saturated condition (Yang and Sato, 2000; Yang, 2004). This deviator stress is able to cause obvious changes in deformation and strength in soil. Therefore, further studies of soil dynamic responses under incident P-waves are of great practical value. To simulate the combined seismic action of simultaneous vertically incident P- and S-waves, Ishihara (1996) superimposed two types of dynamic stresses (Fig. 2c). He expressed dynamic stresses in the form of two shear stress components, $(\sigma_z-\sigma_x)/2$ and τ_{xz}, which show a proportional increase or decrease with seismic action and cause the principal stress direction to deflect by a certain angle β (Fig. 3a). A coordinate system of the two shear stress components $((\sigma_z-\sigma_x)/2-\tau_{xz})$ was introduced, where the stress path is an oblique straight line (Fig. 3b). In a recent experimental earthquake simulation, a cyclic axial force $(\sigma_z-\sigma_x)/2$ and cyclic torque τ_{xz}, were applied to a sample in a dynamic hollow cylinder apparatus (Fig. 4) to simulate the stress path under vertically incident seismic waves (Pan and Chen, 2011).

Vertical incidence is only one special case of seismic wave propagation in the foundation. In recent years, strong earthquakes have occurred frequently, such as the M 8.0 Wenchuan earthquake in China in 2008, the M 8.8 earthquake in Chile in 2010, and the M 9.0 earthquake in eastern Japan in 2011, where strong 3D vibration velocity and acceleration were observed (Li *et al*., 2008; Mimura *et al*., 2011; Boroschek *et al*., 2012). Jin and Liao (1994) obtained seismic wave incidence angles ranging from about

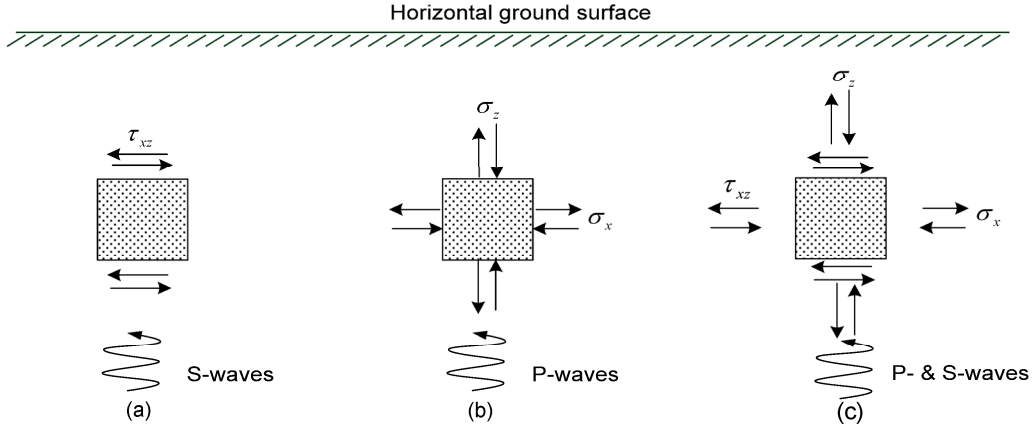

Fig. 2 Seismic stress response of a soil unit in a semi-infinite space under different vertically incident body waves
(a) Shear stresses induced by S-waves; (b) Normal stresses induced by P-waves; (c) Stresses induced by P- and S-waves

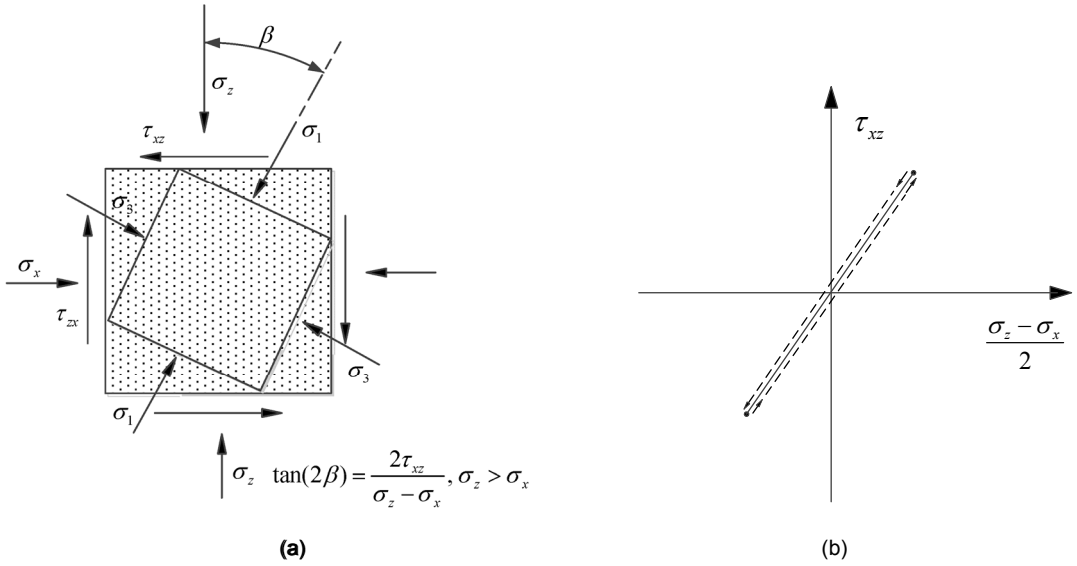

Fig. 3 Rotation of the principal stress direction (a) and stress path (b) induced by vertically incident P- and S-waves
σ_1 is the major principal stress, and σ_3 is the minor principal stress

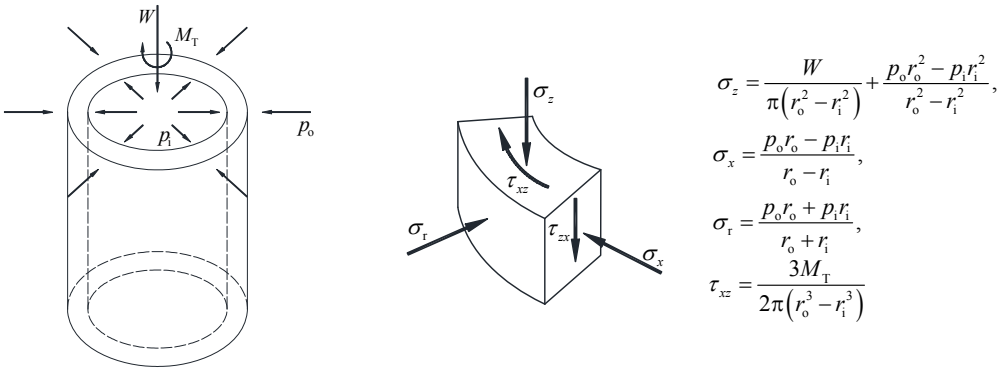

Fig. 4 Working principle of the dynamic hollow cylinder apparatus
W is the axial force, M_T is the torque, p_i is the inner confining pressure, p_o is the outer confining pressure, r_i is the inner diameter, r_o is the outer diameter, and σ_r is the principal stress

45°–75° by regression analysis of 214 surface seismic records in the USA. Takahiro *et al*. (2000) inversely analyzed 24 records of near-field earthquakes in Japan, which indicated that the incidence angle of seismic waves ranged from 12.4°–54.1°. Although the seismic wave incident angle varied greatly, there was no doubt that an oblique incidence of seismic waves leads to a situation in which the movement of a soil unit in the foundation is not just a linear vibration, but an integrated vibration containing swing and vertical components. Furthermore, the ratios between the amplitudes of vibration components in different directions have been proved to be dependent on the angle of incidence (Yang and Sato, 2000).

Results of dynamic tests of a soil unit under a dynamic wave load (Luan *et al.*, 2009) and traffic load (Qian *et al.*, 2013) have amply demonstrated that a dynamic stress path is essential for a dynamic response from the soil. This indicates that a lack of theoretical research on dynamic stress path characteristics of soil under obliquely incident seismic waves is a key constraint to laboratory testing of soil

seismic response. In this paper, based on the theory of elastic waves, dynamic stresses at any depth of a semi-infinite elastic space under obliquely incident P-waves are derived. For the first time, we prove mathematically that under obliquely incident P-waves an oblique elliptic path is formed in a plane consisting of two shear stress components ($(\sigma_z-\sigma_x)/2$ and τ_{xz}). In addition, we systematically analyze the impacts of the incidence angle, Poisson's ratio μ, and depth corresponding to unit wave-length on the shape and size of the elliptic path. The results provide a theoretical reference for further study of the dynamic response of sites under obliquely incident seismic waves.

Due to space limitations, the corresponding analysis of obliquely incident S-waves will be analysed in other study separately.

2 Characteristics of a stress path induced by obliquely incident P-waves

2.1 Seismic stress formula

Based on elastic wave theory (Achenbach, 2012), a bunch of parallel harmonic P-waves with an incident angle α, propagating within the elastic half space, induces reflected P- and SV-waves at the free surface. Ignoring energy attenuation during propagation, the potential function of incident P-waves in a 2D Cartesian coordinate system xoz (Fig. 5) is assumed as

$$\varphi_{-}=A_{-}\exp\left[\mathrm{i}k\left(x\sin\alpha-z\cos\alpha-v_{\mathrm{p}}t\right)\right], \quad (2a)$$

and the potential functions of reflected P- and SV-waves are expressed respectively as

$$\varphi_{+}=A_{+}\exp\left[\mathrm{i}k_1\left(x\sin\beta+z\cos\beta-v_{\mathrm{p}}t\right)\right], \quad (2b)$$

$$\psi_{+}=B_{+}\exp\left[\mathrm{i}k_2\left(x\sin\gamma+z\cos\gamma-v_{\mathrm{s}}t\right)\right], \quad (2c)$$

where i is an imaginary unit; A_{-}, A_{+}, and B_{+} are wave amplitudes; $k=\omega/v_{\mathrm{p}}$, $k_1=\omega_1/v_{\mathrm{p}}$, and $k_2=\omega_2/v_{\mathrm{s}}$ are the wave numbers of incident P-waves, reflected P-waves, and reflected SV-waves, respectively; ω, ω_1, and ω_2 are the respective circular frequencies; v_{s} is the wave velocity of SV-waves equal to $\sqrt{G/\rho}$; v_{p} is the wave velocity of P-waves equal to $\sqrt{(\lambda+2G)/\rho}$, where λ is the Lame constant and G is the shear modulus; α, β, and γ are the respective angles between the propagating direction of corresponding waves and the vertical direction. According to Snell's law, the relationships existing between the parameters are as follows:

$$\begin{cases}\alpha=\beta,\\ k_1=k,\\ \omega=\omega_1=\omega_2,\\ \dfrac{v_{\mathrm{p}}}{v_{\mathrm{s}}}=\dfrac{k_2}{k}=\dfrac{\sin\alpha}{\sin\gamma}=K=\sqrt{\dfrac{2(1-\mu)}{1-2\mu}}.\end{cases} \quad (3)$$

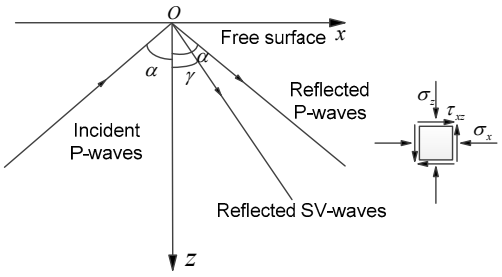

Fig. 5 Reflection of obliquely incident P-waves on a free surface and the seismic stresses applied to soil elements

Using boundary conditions that $\sigma_z=0$ and $\tau_{xz}=0$ when $z=0$, the correlation between the amplitudes of incident and reflected waves can be written as

$$\begin{cases}\dfrac{A_{+}}{A_{-}}=\dfrac{\sin(2\alpha)\sin(2\gamma)-K^2\cos^2(2\gamma)}{\sin(2\alpha)\sin(2\gamma)+K^2\cos^2(2\gamma)},\\ \dfrac{B_{+}}{A_{-}}=\dfrac{-2\sin(2\alpha)\cos(2\gamma)}{\sin(2\alpha)\sin(2\gamma)+K^2\cos^2(2\gamma)}.\end{cases} \quad (4)$$

The potential function of displacement is expressed as

$$\begin{Bmatrix}u_x\\ u_z\end{Bmatrix}=\begin{Bmatrix}\dfrac{\partial}{\partial x}\\ \dfrac{\partial}{\partial z}\end{Bmatrix}\varphi+\begin{Bmatrix}-\dfrac{\partial}{\partial z}\\ \dfrac{\partial}{\partial x}\end{Bmatrix}\psi, \quad (5)$$

where $\varphi=\varphi_{-}+\varphi_{+}$, $\psi=\psi_{+}$. According to Hooke's law, seismic stresses generated by incident and reflected plane waves at any point in the foundation can be obtained as follows:

$$\begin{cases}\sigma_x=\lambda\left(\dfrac{\partial u_x}{\partial x}+\dfrac{\partial u_z}{\partial z}\right)+2G\dfrac{\partial u_x}{\partial x},\\ \sigma_z=\lambda\left(\dfrac{\partial u_x}{\partial x}+\dfrac{\partial u_z}{\partial z}\right)+2G\dfrac{\partial u_z}{\partial z},\\ \tau_{xz}=G\left(\dfrac{\partial u_x}{\partial z}+\dfrac{\partial u_z}{\partial x}\right).\end{cases} \tag{6}$$

2.2 Pattern of seismic stress path under obliquely incident P-waves

Combining Eqs. (2)–(6), the time history of stresses induced at any point within the semi-space due to the inclined incident P-waves can be obtained. The characteristic variation of stresses in a soil element was further investigated.

For seeking the general rule, seismic stress components in Eq. (6) are normalized as $\frac{\sigma_x}{A\_\rho\omega^2}$, $\frac{\sigma_z}{A\_\rho\omega^2}$, and $\frac{\tau_{xz}}{A\_\rho\omega^2}$, where $A\_\rho\omega^2$ reflects the incident energy density.

However, it is difficult to apply these three seismic stress components simultaneously using the current dynamic test apparatus. Up to now, these three cyclic loads have often been simplified as cyclic axial normal stress and cyclic horizontal torsional shear stress, simulated in a hollow cylinder apparatus (HCA). This simplified method was adopted by Ishihara and Towhata (1983) to simulate ocean wave loads, and by Qian *et al*. (2013) to simulate traffic loads. Therefore, with reference to their work, setting $X=\frac{\sigma_z-\sigma_x}{2A\_\rho\omega^2}$ and $Y=\frac{\tau_{xz}}{A\_\rho\omega^2}$, the expressions for σ_x, σ_z, and τ_{xz} can be combined and rewritten as follows:

$$X=M_1\sin\xi+M_2\cos\xi, \tag{7a}$$

$$Y=N_1\sin\xi+N_2\cos\xi, \tag{7b}$$

where $\xi=k(x\sin\alpha-v_pt)=k_2(x\sin\gamma-v_st)$ and the coefficients M_1, M_2, N_1, and N_2 are expressed as

$$M_1=-4\csc\alpha\sin^2\gamma\cos(2\gamma)\left(\cos(2\alpha)\cos(2\gamma)\sin\chi+\sin(2\alpha)\cdot\sin(2\gamma)\sin\kappa\right)\frac{1}{\sin\alpha+2\cos\alpha\sin(2\gamma)+\sin(\alpha-4\gamma)}, \tag{8a}$$

$$M_2=\left(4\cos\alpha\sin^2\gamma\sin(4\gamma)\cos\kappa-8\csc^2\alpha\cos\alpha\sin^4\gamma\sin(2\gamma)\cdot\cos(2\alpha)\cos\chi\right)\frac{1}{\sin\alpha+2\cos\alpha\sin(2\gamma)+\sin(\alpha-4\gamma)}, \tag{8b}$$

$$N_1=\left(16\csc\alpha\cos^2\alpha\sin^4\gamma\sin(2\gamma)\sin\chi+8\cos\alpha\sin^2\gamma\cdot\cos^2(2\gamma)\sin\kappa\right)\frac{1}{\sin\alpha+2\cos\alpha\sin(2\gamma)+\sin(\alpha-4\gamma)}, \tag{8c}$$

$$N_2=\frac{8\sin^2\gamma\cos\alpha\cos^2(2\gamma)(\cos\chi-\cos\kappa)}{\sin\alpha+2\cos\alpha\sin(2\gamma)+\sin(\alpha-4\gamma)}, \tag{8d}$$

where $\chi=kz\cos\alpha$, $\kappa=kz\cot\gamma\sin\alpha$.

Combining Eqs. (7a) and (7b), $\sin\xi=\frac{N_2X-M_2Y}{M_1N_2-M_2N_1}$ and $\cos\xi=\frac{N_1X-M_1Y}{M_2N_1-M_1N_2}$ will be given. Substituting these expressions of $\sin\xi$ and $\cos\xi$ into the equation $\sin^2\xi+\cos^2\xi=1$ yields:

$$\frac{N_1^2+N_2^2}{\left(M_2N_1-M_1N_2\right)^2}X^2+\frac{M_1^2+M_2^2}{\left(M_2N_1-M_1N_2\right)^2}Y^2+\frac{-2\left(M_1N_1+M_2N_2\right)}{\left(M_2N_1-M_1N_2\right)^2}XY=1. \tag{9}$$

Mathematically, the general form and corresponding condition of an oblique ellipse formula is expressed as

$$Ax^2+By^2+2Cxy=1,\ C^2-AB<0. \tag{10}$$

For any SV-waves exit angle γ not equal to zero, $M_2N_1-M_1N_2\neq0$ can always be deduced from Eq. (8). Thus, the corresponding condition $C^2-AB=-\frac{1}{\left(M_2N_1-M_1N_2\right)^2}<0$ will hold. It can be inferred that Eq. (9) (compared with Eq. (10)) is a function of an oblique ellipse, which proves that the dynamic stress path generated by single obliquely incident P-waves is an oblique ellipse.

Any oblique ellipse can also be expressed as

$$\frac{1}{L_a^2}\left[\left(\cos^2\theta+\frac{\sin^2\theta}{\delta^2}\right)X^2+\left(\sin^2\theta+\frac{\cos^2\theta}{\delta^2}\right)Y^2+2\left(\cos\theta\sin\theta-\frac{\cos\theta\sin\theta}{\delta^2}\right)XY\right]=1, \tag{11}$$

where $2L_a$ is the length of the long axis, representing the size of the ellipse; θ is the polarization angle between the long axis and the positive x axis (Fig. 6); δ is the ellipticity, the ratio of the length of the short axis to the length of the long axis, ranging between 0 and 1. The inclination of the ellipse is represented by θ and the flatness by δ. The formula in square brackets applies to a unit ellipse with polarization angle θ and ellipticity δ. θ, δ, and L_a are the three characteristic parameters of any oblique ellipse.

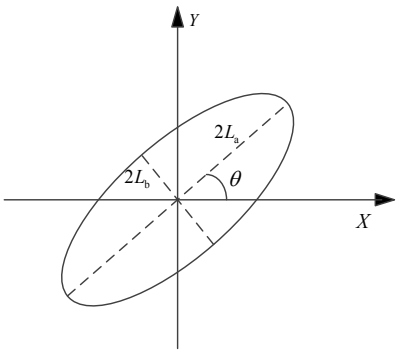

Fig. 6 Oblique ellipse geometrical characteristic parameters demonstration

Similarly, the oblique ellipse represented by Eq. (9) can be rewritten in the form of Eq. (11). Then, the characteristic parameters of oblique elliptic stress paths induced by obliquely incident P-waves can be obtained. Due to space limitations, the expressions for the characteristic parameters L_a, θ, δ, and the derivation details are given in Appendix A (Eqs. (A12)–(A14)). Once the three characteristic parameters have been determined, the magnitudes of the cyclic axial stress and horizontal shear stress, as well as their phase differences, can be determined. These are required for the laboratory tests used to simulate the oblique elliptic stress path.

3 Analysis of factors affecting the oblique elliptic stress path

From Eqs. (A12)–(A14) in Appendix A, it can be deduced that the characteristic parameters L_a, θ, and δ are influenced by various factors, including the incident angle α, Poisson's ratio μ, seismic wave frequency f, wave velocity v_s or v_p, and the depth z. The incident angle α and Poisson's ratio μ are relatively independent physical parameters. However, although wave frequency and wave velocity reflect characteristics of seismic waves and soil, respectively, their impacts on the stress path pattern are coupled and mutually interactive. With dimensional analysis, the dimensionless factor zf/v_s is introduced, which is able to reflect the integrative impact of depth, frequency, and wave velocity on L_a, θ, and δ. Shear wavelength can be represented as v_s/f, thus zf/v_s stands for the depth corresponding to unit wavelength. Moreover, considering that shear wave velocity is a vital parameter used in geotechnical engineering prospecting for depicting the mechanical behavior of a soil medium, v_s was chosen rather than v_p. In this section, the impacts of these three factors (α, μ, and zf/v_s) on the elliptic stress path are analyzed and discussed in detail, with curves plotted following numerical computation to describe those impacts.

3.1 Impact of incident angle on the shape of the elliptic stress path

Allen and Kanamori (2003) provided a formula for estimating the dominant frequency of seismic P-waves, which has been found to be in the range of 0.5–2.15 Hz for earthquakes of magnitudes 5–8. The actual depth at which liquefaction in possible is generally within 30 m, where the shear wave velocity v_s ranges from 100–480 m/s (Liu *et al.*, 2010). The range of zf/v_s in this study was about 0–0.8, which was broadened to a depth of unit wavelength considering the complexity of earthquakes. Thus, the correlation between θ or δ and zf/v_s for different incident angles α of P-waves can be plotted. Several typical curves given μ=0.4 are illustrated in Fig. 7, where 1° represents the situation of approximately vertical incidence, and 10° and 30° represent a situation of relatively small incident angles. 60° represents the remaining situation of all incident angles bigger than 45° because in this range the patterns of the different curves are essentially similar.

In Fig. 7a, θ=0° means that the direction of the long axis of the ellipse is in the horizontal axis direction in the plane of X and Y, θ<0° means it rotates clockwise from θ=0°, while θ>0° means that rotation

is anticlockwise. It can be found that θ is nearly 0° when α=1°, and almost unchanged with the development of zf/v_s. That means only a normal stress difference is generated and shear stress can be ignored when P-waves are vertically incident, which is consistent with general knowledge. In the other conditions, θ declines from 0° to a negative peak before increasing gradually with the development of zf/v_s. With different incident angles, different negative peaks and different angles will be reached by the long axis rotating counterclockwise. When the incident angle is around 30°, θ arrives at a negative peak of about –90°. When the incident angle is around 10°, θ may even increase back to a positive angle of around 90°. It can be inferred that the value of θ covers almost the whole range (i.e., −90°–90°) with the variation in the incident angle of the seismic P-waves.

In Fig. 7b, δ reaches several peaks with the change in zf/v_s. Curves of large incident angles (>45°) have similar patterns of adjacent bulgy hills, as represented by the curve of incident angle 60° in Fig. 7b. The greater the incident angle, the higher the corresponding peak values of δ. All δ values decline to 0 when zf/v_s is around 0.45. For small incident angles, the points of δ=0 are at about zf/v_s=0.7–0.8. For incident angles of 1°, 10°, and 30° (Fig. 7b), curves of δ with zf/v_s are all in the shape of an asymmetric saddle before δ declines to 0. The peak value of δ is referred to as the maximum ellipticity of the stress path. δ=0 refers to the shape of the stress path as an oblique line transformed from a normal oblique ellipse (Fig. 8), which means that the principal direction of stress in the soil element does not rotate continually but stepwise, in steps of 90°. From Eqs. (A9)–(A11) and (A13), it is found that M_1N_2=M_2N_1 holds for the situation above, when taking a certain value of zf/v_s. Thus, the phases of the two stress components $(\sigma_z-\sigma_x)/2$ and τ_{xz} are reversed, which means the phase difference is π. The pattern of the stress path approaches a circle when δ increases. The peak value of δ in the study reached 0.973, when the stress path was almost a circle, with the deviatoric stress unchanged and continual rotation of its principal stress direction, similar to that induced by wave loads (Ishihara and Towhata, 1983). The stress path generated by obliquely incident P-waves has been proved to be obliquely elliptic, but it is still able to change from a line to a circle with a particular combination of depth, frequency, and shear wave velocity, creating quite diverse patterns.

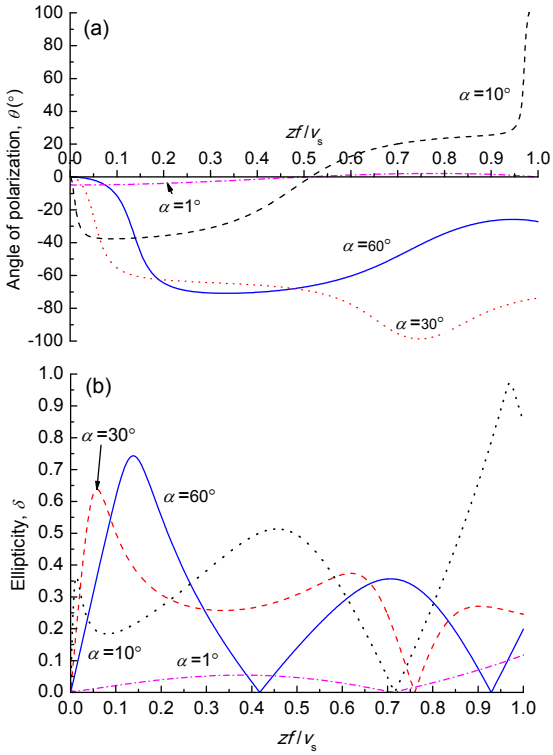

Fig. 7 Typical curves of oblique ellipse shape parameters against zf/v_s when μ=0.4

(a) Typical curves of θ against zf/v_s; (b) Typical curves of δ against zf/v_s

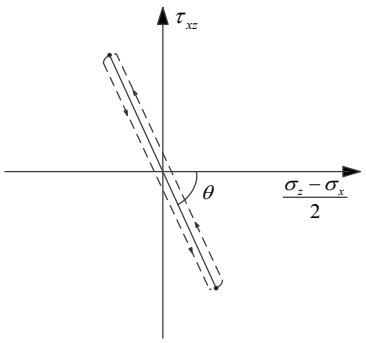

Fig. 8 Dynamic stress path when δ=0

3.2 Impact of Poisson's ratio on the shape of the elliptic stress path

In Section 3.1, different patterns of θ and δ are presented for P-waves with incident angles of α>30° and <30°. The impact of Poisson's ratio μ on θ and δ was investigated. Given α=10° or 60° as examples,

the change of θ and δ with zf/v_s varying was analyzed (Figs. 9 and 10). The degree of saturation of the soil is related to Poisson's ratio. The greater the Poisson's ratio, the greater is the soil saturation. Yoshimi *et al.* (1989) provided evidence demonstrating that liquefaction resistance at 70% saturation is about three times that at full saturation. Therefore, this paper considers only soil with a degree of saturation of more than 70%, which is probably liquefied. Yang and Sato (2000)'s research on soil saturation and Poisson's ratio showed that when saturation is between 70% and 100%, Poisson's ratio of soil is about 0.3–0.5. Considering the denominator of the algebraic expression of K in Eq. (3) cannot be zero, we chose Poisson's ratios ranging from 0.3 to 0.48.

Given different Poisson's ratios, curves of elliptic θ changing with zf/v_s were drawn (Figs. 9a and 9b) when the incident angle of the P-waves is 10° or 60°, respectively. When the ellipse is rotated continually clockwise through 180° in two steps, then the direction of the long axis is consistent with that of the horizontal axis again when α=10° and μ=0.48. The remaining curves all demonstrate that the ellipse rotates back after θ increases back until reaching the negative peak with zf/v_s developing. To sum up, the polarization angle θ of an obliquely elliptic stress path is influenced greatly by the Poisson's ratio when the incident angle is small and the soil nearly fully saturated, while in the remaining conditions, although it affects the negative peak and the point where the ellipse rolls back, it barely affects the pattern of θ. With a greater Poisson's ratio, the ellipse can deflect by a greater angle. The greater the Poisson's ratio, the higher the peak of δ that will be reached (Fig. 10). Nevertheless, the pattern of δ curves also remains unchanged, which do not need repeat.

In laboratory dynamic tests on soil, to simulate the required stress path, zf/v_s can be determined roughly by measuring the shear wave velocity and the buried depth of soil, and the ranges of θ and δ can then be fixed according to the curves in Figs. 7, 9, and 10.

3.3 Impact of related factors on the size of the elliptic stress path

In a dimensionless obliquely elliptic stress path under obliquely incident P-waves, L is the distance

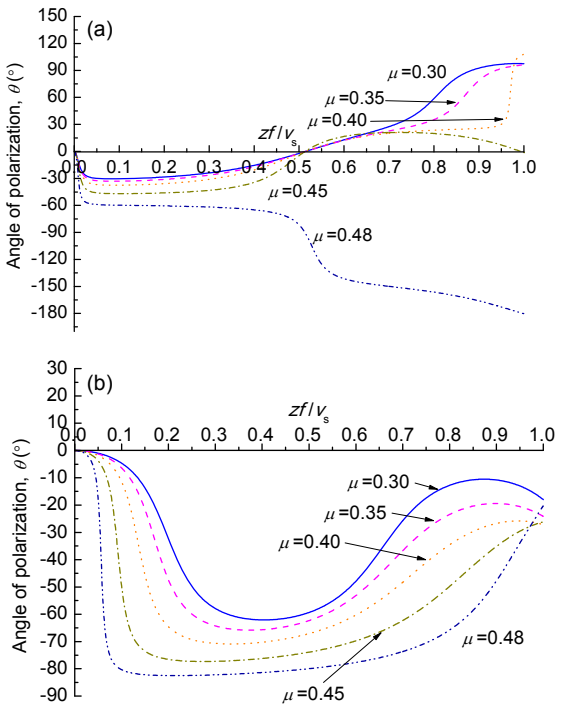

Fig. 9 Typical curves of θ against zf/v_s at different Poisson's ratios when α=10° (a) or 60° (b)

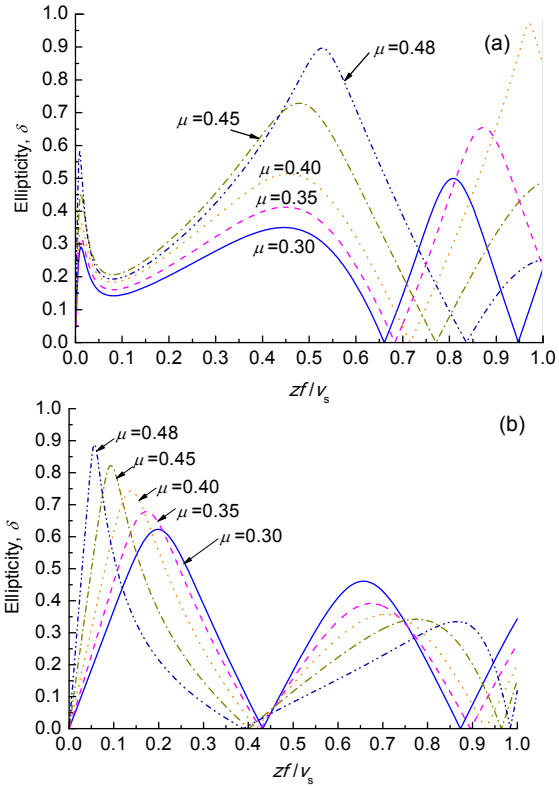

Fig. 10 Typical curves of δ against zf/v_s at different Poisson's ratios when α=10° (a) or 60° (b)

between the origin of the coordinates and any point on the ellipse (Fig. 11). According to geometry relationships:

$$L=\sqrt{\left(\frac{\sigma_z-\sigma_x}{2A\_\rho\omega^2}\right)^2+\left(\frac{\tau_{xz}}{A\_\rho\omega^2}\right)^2}, \tag{12}$$

and the deviatoric stress defined by the difference between the major and minor principal stresses is expressed as

$$\frac{\sigma_1-\sigma_3}{2}=\sqrt{\left(\frac{\sigma_z-\sigma_x}{2}\right)^2+\tau_{xz}^2}. \tag{13}$$

This describes the combined action of a normal stress difference and horizontal shear stress under complex stress paths, and therefore the magnitudes of dynamic stresses can be reflected by L. The value of deviatoric stress varies within a single cycle, and will arrive at its maximum value when $L=L_a$ and minimum value when $L=L_b$. Thus, under unit incident energy, half the length of long axis L_a can be used to represent the dynamic stress level in an earthquake. By taking a value of the incident angle close to zero, dynamic deviatoric stresses under vertical incidence can also be calculated. If Poisson's ratio is also taken as zero, this will degenerate into 1D vibration of a rigid body, and only vertical displacement u_z will be produced. Correspondingly, vertically incident SV-waves will produce only horizontal displacement u_x, which is the basic assumption of the Seed-Idriss simplified procedure for evaluating stresses induced by earthquakes. Thus, Seed-Idriss's procedure can be seen as a special case of the elastic method described in this paper.

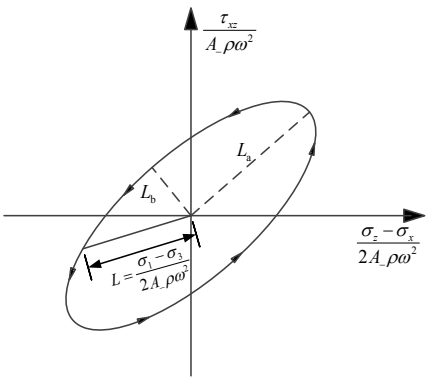

Fig. 11 Deviatoric stresses of an oblique elliptic stress path in any single cycle

In Fig. 12, L_a is plotted with variable zf/v_s. The incident angles are divided into three categories: nearly vertical incidence (1°, 5°, and 10°), oblique incidence (30°, 45°, and 60°), and nearly horizontal incidence (80°, 85°, and 89°) for investigation. L_a is the highest with oblique incidence, which corresponds to the highest seismic dynamic stress level in

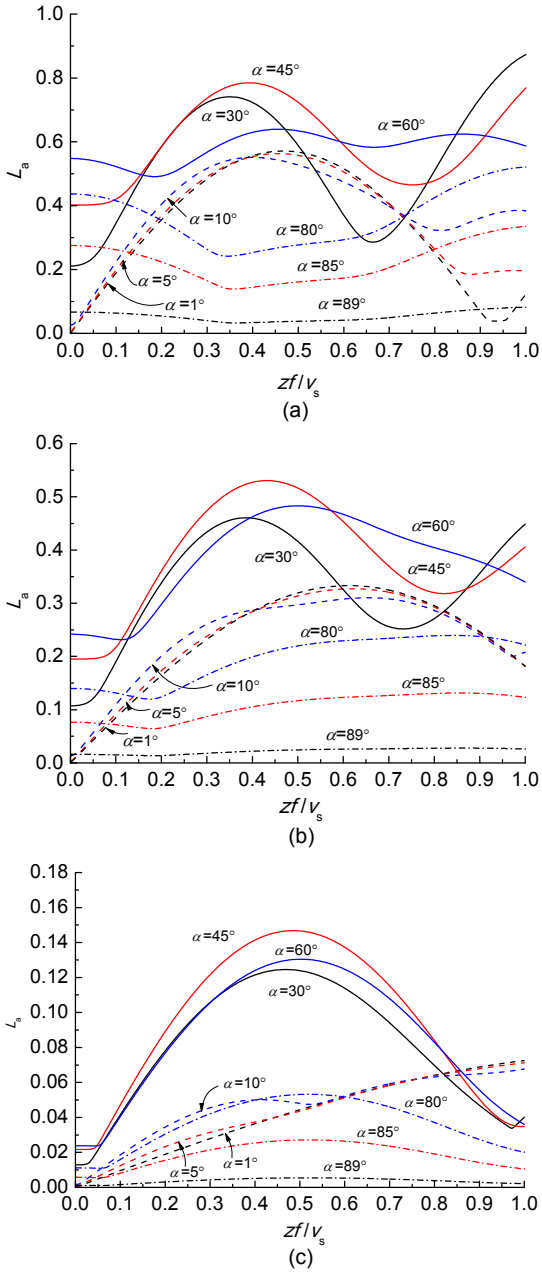

Fig. 12 L_a develops with zf/v_s varying at different α
(a) μ=0.3, 70% degree of saturation; (b) μ=0.4, 99% degree of saturation; (c) μ=0.48, full saturation

the soil. For the two other categories of incident angles, the seismic dynamic stress level of the soil is relatively low, especially for horizontal incidence. Thus, it is much more dangerous when P-waves are obliquely incident, while the safest condition occurs when P-waves are horizontally incident.

Three typical values of Poisson's ratio were taken to simulate different degrees of saturation: μ=0.3 corresponds to a low degree of saturation of about 70%, μ=0.4 corresponds to a high degree of saturation of about 99%, and μ=0.48 corresponds to full saturation. In the most dangerous condition when P-waves are obliquely incident, the lower the degree of saturation of the soil, the greater the value of L_a, which approaches 0.8. Increasing Poisson's ratio makes different L_a values more discrete. When μ=0.48, L_a under incident angles between 30° and 60° is much greater and the level of dynamic stresses is more than twice that of other incident angles.

4 Conclusions

Based on elastic wave theory with appropriate simplification for seismic waves, dynamic stresses in foundation soil generated by obliquely incident P-waves have been derived. This has revealed the characteristics of the corresponding dynamic stress path which has been mathematically proved to be an oblique ellipse in the plane of $(\sigma_z-\sigma_x)/2$ and τ_{xz}. Both a circular path and a straight line path can be regarded as special cases of an oblique ellipse. The shape and size of obliquely elliptic stress path are affected by three independent factors including incident angle, Poisson's ratio, and depth corresponding to unit wavelength. When soil is not close to full saturation, but with a degree of saturation of more than 70%, Poisson's ratio will hardly make any great difference to the shape of an oblique elliptic stress path in foundation soil. Once the incident angle extends beyond 45°, the path is mainly in the shape of a vertical oblate ellipse and remains almost unchanged with variation in the incident angle. Half the length of the elliptic long axis L_a is equal to the maximum deviatoric stress generated by P-waves, which can reflect the dynamic stress level under seismic waves. With an increase in Poisson's ratio within 0.3–0.48, the half long axis length declines notably. When the P-wave incident angle is within the range 30°–60°, the induced dynamic deviatoric stresses will reach their maximum value. In particular, when Poisson's ratio is 0.48, the stress amplitudes are more than twice those under other incident angles.

This study shows that for oblique incidence, the dynamic stress path under P-waves has a changeable shape and the dynamic stress level is possibly higher. Therefore, considering only vertically incident seismic waves is not sufficient to cover the most dangerous earthquake conditions, and the study of soil dynamic stress response under obliquely incident P-waves is necessary.

References

Achenbach, J., 2012. Wave Propagation in Elastic Solids. Elsevier Publishing Company Inc., New York, USA, p.165-198.

Allen, R.M., Kanamori, H., 2003. The potential for earthquake early warning in southern California. *Science*, **300**(5620): 786-789. http://dx.doi.org/10.1126/science.1080912

Boroschek, R.L., Contreras, V., Kwak, D.Y., *et al.*, 2012. Strong ground motion attributes of the 2010 Mw 8.8 Maule, Chile, earthquake. *Earthquake Spectra*, **28**(S1): S19-S38. http://dx.doi.org/10.1193/1.4000045

Ding, H., 2010. Experimental Study of the Dynamics of Saturated Sand Subjected to Incident Seismic Waves. MS Thesis, Zhejiang University, Hangzhou, China (in Chinese).

Gu, C., Cai, Y., Wang, J., 2012. Coupling effects of P-waves and S-waves based on cyclic triaxial tests with cyclic confining pressure. *Chinese Journal of Geotechnical Engineering*, **34**(10):1903-1909 (in Chinese).

Gubbins, D., Snieder, R., 1991. Dispersion of P waves in subducted lithosphere: evidence for an eclogite layer. *Journal of Geophysical Research: Solid Earth*, **96**(B4): 6321-6333. http://dx.doi.org/10.1029/90JB02741

Ishihara, K., 1996. Soil Behaviour in Earthquake Geotechnics. Oxford University Press, Oxford, UK, p.6-15.

Ishihara, K., Towhata, I., 1983. Sand response to cyclic rotation of principal stress directions as induced by wave loads. *Japanese Society of Soil Mechanics and Foundation Engineering*, **23**(4):11-26.

Jin, X., Liao, Z., 1994. Statistical research on S-wave incident angle. *Earthquake Research in China*, **8**(1):121-131.

Li, N., Huang, B., Ling, D., *et al.*, 2015. Experimental research on behaviors of saturated loose sand subjected to oblique ellipse stress path. *Rock and Soil Mechanics*, **36**(1): 156-170 (in Chinese). http://dx.doi.org/10.16285/j.rsm.2015.01.022

Li, X., Zhou, Z., Yu, H., *et al.*, 2008. Strong motion observations and recordings from the great Wenchuan Earthquake. *Earthquake Engineering and Engineering Vibration*, **7**(3):235-246. http://dx.doi.org/10.1007/s11803-008-0892-x

Liu, H., Zheng, T., Bo, J., *et al.*, 2010. Statistical analysis of uncertainty for shear wave velocities of cohesive soils. *World Information on Earthquake Engineering*, **26**(S1): 99-103 (in Chinese).

Luan, M., Nie, Y., Yang, Q., *et al.*, 2009. Study of coupling cyclic test of saturated clay under different stress paths. *Rock and Soil Mechanics*, **30**(7):1927-1932 (in Chinese).

Mimura, N., Yasuhara, K., Kawagoe, S., *et al.*, 2011. Damage from the Great East Japan Earthquake and Tsunami-a quick report. *Mitigation and Adaptation Strategies for Global Change*, **16**(7):803-818. http://dx.doi.org/10.1007/s11027-011-9297-7

Pan, H., Chen, G., 2011. Analysis of capabilities of HCA to simulate stress paths for principal stress rotation under dynamic confining pressure. *Rock and Soil Mechanics*, **32**(6):1701-1706 (in Chinese).

Qian, J., Wang, Y., Zhang, J., *et al.*, 2013. Undrained cyclic torsion shear tests on permanent deformation responses of soft saturated clay to traffic loadings. *Chinese Journal of Geotechnical Engineering*, **35**(10):1790-1798 (in Chinese).

Seed, H.B., Lee, K.L., 1966. Liquefaction of saturated sands during cyclic loading. *Journal of the Soil Mechanics and Foundations Division, ASCE*, **92**(6):105-134.

Seed, H.B., Peacock, W.H., 1971. Test procedures for measuring soil liquefaction characteristics. *Journal of the Soil Mechanics and Foundations Division, ASCE*, **97**(8): 1099-1119.

Seed, H.B., Idriss, I.M., 1971. Simplified procedure for evaluating soil liquefaction potential. *Journal of the Soil Mechanics and Foundations Division, ASCE*, **97**(9): 1249-1273.

Seed, H.B., Idriss, I.M., Arango, I., 1983. Evaluation of liquefaction potential using field performance data. *Journal of Geotechnical Engineering*, **109**(3):458-482. http://dx.doi.org/10.1061/(ASCE)0733-9410(1983)109:3(458)

Takahiro, S., Kazuhiko, K., Yoichi, S., *et al.*, 2000. Estimation of earthquake motion incident angle at rock site. Proceedings of 12th World Conference on Earthquake Engineering, Paper No. 0956.

Thiers, G.R., Seed, H.B., 1968. Cyclic stress-strain characteristics of clays. *Journal of Soil Mechanics and Foundations*, **94**(2):555-569.

Yang, J., 2000. Influence of water saturation on horizontal and vertical motion at a porous soil interface induced by incident P wave. *Soil Dynamics and Earthquake Engineering*, **19**(8): 575-581. http://dx.doi.org/10.1016/S0267-7261(00)00067-1

Yang, J., 2004. Reappraisal of vertical motion effects on soil liquefaction. *Géotechnique*, **54**(10):671-676. http://dx.doi.org/10.1680/geot.2004.54.10.671

Yang, J., Sato, T., 2000. Interpretation of seismic vertical amplification observed at an array site. *Bulletin of the Seismological Society of America*, **90**(2):275-285. http://dx.doi.org/10.1785/0119990068

Yoshimi, Y., Tanaka, K., Tokimatsu, K., 1989. Liquefaction resistance of a partially saturated sand. *Soils and Foundations*, **29**(3):157-162. http://dx.doi.org/10.3208/sandf1972.29.3_157

You, H., Zhao, F., Rong, M., 2009. Nonlinear seismic response of horizontal layered site due to inclined wave. *Chinese Journal of Geotechnical Engineering*, **31**(2):234-240 (in Chinese).

Appendix A

The size of a general oblique ellipse depends on the long axis length, and its shape and orientation can be described by the polarization angle and ellipticity (Fig. 6). The polarization angle is the angle between the long axis and the positive direction of the X axis (counterclockwise is positive). The value of ellipticity reflects whether the ellipse is slender or circular in shape. In the general formula of an ellipse (Eq. (10)), the coefficients A, B, and C determine its shape.

Likewise, the size and shape of the stress path depend on the corresponding coefficients in Eq. (9). Setting $A=\dfrac{N_1^2+N_2^2}{\left(M_2N_1-M_1N_2\right)^2}$, $B=\dfrac{M_1^2+M_2^2}{\left(M_2N_1-M_1N_2\right)^2}$, and $C=-\dfrac{M_1N_1+M_2N_2}{\left(M_2N_1-M_1N_2\right)^2}$, Eq. (9) can be rewritten as

$$AX^2+BY^2+2CXY=1. \tag{A1}$$

If the original coordinate (x, y) is rotated clockwise by an angle of θ to the new coordinate (X, Y), the standard ellipse originally expressed as $\dfrac{x^2}{L_a^2}+\dfrac{y^2}{L_b^2}=1$

transforms to $\frac{1}{L_a^2}(X\cos\theta+Y\sin\theta)^2+\frac{1}{L_b^2}(-X\sin\theta+Y\cos\theta)^2=1$ experiencing a counterclockwise rotation by the same angle, which can be rewritten as

$$\left(\frac{\cos^2\theta}{L_a^2}+\frac{\sin^2\theta}{L_b^2}\right)X^2+\left(\frac{\sin^2\theta}{L_a^2}+\frac{\cos^2\theta}{L_b^2}\right)Y^2+2\left(\frac{\cos\theta\sin\theta}{L_a^2}-\frac{\cos\theta\sin\theta}{L_b^2}\right)XY=1. \tag{A2}$$

Combining Eq. (A1) with Eq. (A2) yields:

$$A=\frac{\cos^2\theta}{L_a^2}+\frac{\sin^2\theta}{L_b^2}, \tag{A3a}$$

$$B=\frac{\sin^2\theta}{L_a^2}+\frac{\cos^2\theta}{L_b^2}, \tag{A3b}$$

$$C=\frac{\cos\theta\sin\theta}{L_a^2}-\frac{\cos\theta\sin\theta}{L_b^2}. \tag{A3c}$$

Subtracting Eq. (A3a) by Eq. (A3b) gives $A-B=\left(\frac{1}{L_a^2}-\frac{1}{L_b^2}\right)\cos(2\theta)$; adding Eq. (A3a) to Eq. (A3b) gives $A+B=\frac{1}{L_a^2}+\frac{1}{L_b^2}$. Eq. (A3c) can be simplified as $2C=\left(\frac{1}{L_a^2}-\frac{1}{L_b^2}\right)\sin(2\theta)$.

Combining the results above, the polarization angle is determined by Eq. (A4):

$$\sin(2\theta)=\frac{2C}{-\sqrt{(A-B)^2+4C^2}}, \tag{A4a}$$

and

$$\cos(2\theta)=\frac{A-B}{-\sqrt{(A-B)^2+4C^2}}. \tag{A4b}$$

The double axes length and ellipticity are also derived as

$$\frac{1}{L_a^2}=\frac{1}{2}\left(A+B-\sqrt{(A-B)^2+4C^2}\right), \tag{A5}$$

$$\frac{1}{L_b^2}=\frac{1}{2}\left(A+B+\sqrt{(A-B)^2+4C^2}\right), \tag{A6}$$

and

$$\delta^2=\frac{L_b^2}{L_a^2}=\frac{A+B-\sqrt{(A-B)^2+4C^2}}{A+B+\sqrt{(A-B)^2+4C^2}}. \tag{A7}$$

Eq. (A2) is rewritten as

$$\frac{1}{L_a^2}\left[\left(\cos^2\theta+\frac{\sin^2\theta}{\delta^2}\right)X^2+\left(\sin^2\theta+\frac{\cos^2\theta}{\delta^2}\right)Y^2+2\left(\cos\theta\sin\theta-\frac{\cos\theta\sin\theta}{\delta^2}\right)XY\right]=1, \tag{A8}$$

which is the same as Eq. (11). The derivations of analytical expressions of A, B, and C are shown in Eqs. (A9)–(A11):

$$\begin{aligned}&N_1^2+N_2^2\\&=\left\{\left[16\csc\alpha\cos^2\alpha\sin^4\gamma\sin(2\gamma)\sin\chi+8\cos\alpha\sin^2\gamma\cos^2(2\gamma)\sin\kappa\right]^2+\left[8\sin^2\gamma\cos\alpha\cos^2(2\gamma)\right.\right.\\&\left.\left.\cdot(\cos\chi-\cos\kappa)\right]^2\right\}\Big/\left[\sin\alpha+2\cos\alpha\sin(2\gamma)+\sin(\alpha-4\gamma)\right]^2,\\&M_1^2+M_2^2\\&=\left\{\left[-4\csc\alpha\sin^2\gamma\cos(2\gamma)\left(\cos(2\alpha)\cos(2\gamma)\sin\chi+\sin(2\alpha)\sin(2\gamma)\sin\kappa\right)\right]^2+\left[4\cos\alpha\sin^2\gamma\sin(4\gamma)\cos\kappa\right.\right.\\&\left.\left.-8\csc^2\alpha\cos\alpha\sin^4\gamma\sin(2\gamma)\cos(2\alpha)\cos\chi\right]^2\right\}\Big/\left[\sin\alpha+2\cos\alpha\sin(2\gamma)+\sin(\alpha-4\gamma)\right]^2,\end{aligned}$$

$$
\begin{aligned}
&M_1N_1+M_2N_2\\
&=\Big[-4\csc\alpha\sin^2\gamma\cos(2\gamma)\big(\cos(2\alpha)\cos(2\gamma)\sin\chi+\sin(2\alpha)\sin(2\gamma)\sin\kappa\big)\big(16\csc\alpha\cos^2\alpha\sin^4\gamma\sin(2\gamma)\sin\chi\\
&\quad+8\cos\alpha\sin^2\gamma\cos^2(2\gamma)\sin\kappa\big)+8\sin^2\gamma\cos\alpha\cos^2(2\gamma)\big(\cos\chi-\cos\kappa\big)\big(4\cos\alpha\sin^2\gamma\sin(4\gamma)\cos\kappa\\
&\quad-8\csc^2\alpha\cos\alpha\sin^4\gamma\sin(2\gamma)\cos(2\alpha)\cos\chi\big)\Big]\Big/\big[\sin\alpha+2\cos\alpha\sin(2\gamma)+\sin(\alpha-4\gamma)\big]^2,\\
&M_2N_1-M_1N_2\\
&=\Big[\big(4\cos\alpha\sin^2\gamma\sin(4\gamma)\cos\kappa-8\csc^2\alpha\cos\alpha\sin^4\gamma\sin(2\gamma)\cos(2\alpha)\cos\chi\big)\big(16\csc\alpha\cos^2\alpha\sin^4\gamma\\
&\quad\cdot\sin(2\gamma)\sin\chi+8\cos\alpha\sin^2\gamma\cos^2(2\gamma)\sin\kappa\big)+32\csc\alpha\cos\alpha\sin^2\gamma\cos(2\gamma)\sin^2\gamma\cos^2(2\gamma)\\
&\quad\cdot\big(\cos(2\alpha)\cos(2\gamma)\sin\chi+\sin(2\alpha)\sin(2\gamma)\sin\kappa\big)\big(\cos\chi-\cos\kappa\big)\Big]\Big/\big[\sin\alpha+2\cos\alpha\sin(2\gamma)+\sin(\alpha-4\gamma)\big]^2,\\
&A=\frac{N_1^2+N_2^2}{\big(M_2N_1-M_1N_2\big)^2}\\
&\quad=\big[\sin\alpha+2\cos\alpha\sin(2\gamma)+\sin(\alpha-4\gamma)\big]^2\Big\{\Big[16\csc\alpha\cos^2\alpha\sin^4\gamma\sin(2\gamma)\sin\chi+8\cos\alpha\sin^2\gamma\\
&\qquad\cdot\cos^2(2\gamma)\sin\kappa\Big]^2+\Big[8\sin^2\gamma\cos\alpha\cos^2(2\gamma)\big(\cos\chi-\cos\kappa\big)\Big]^2\Big\}\Big/\Big[\big(4\cos\alpha\sin^2\gamma\sin(4\gamma)\cos\kappa-8\csc^2\alpha\cos\alpha\\
&\qquad\cdot\sin^4\gamma\sin(2\gamma)\cos(2\alpha)\cos\chi\big)\big(16\csc\alpha\cos^2\alpha\sin^4\gamma\sin(2\gamma)\sin\chi+8\cos\alpha\sin^2\gamma\cos^2(2\gamma)\sin\kappa\big)\\
&\qquad+32\csc\alpha\cos\alpha\sin^2\gamma\cos(2\gamma)\sin^2\gamma\cos^2(2\gamma)\big(\cos(2\alpha)\cos(2\gamma)\sin\chi+\sin(2\alpha)\sin(2\gamma)\sin\kappa\big)\big(\cos\chi-\cos\kappa\big)\Big]^2,
\end{aligned}
\tag{A9}
$$

$$
\begin{aligned}
&B=\frac{M_1^2+M_2^2}{\big(M_2N_1-M_1N_2\big)^2}\\
&\quad=\big[\sin\alpha+2\cos\alpha\sin(2\gamma)+\sin(\alpha-4\gamma)\big]^2\Big\{\Big[-4\csc\alpha\sin^2\gamma\cos(2\gamma)\big(\cos(2\alpha)\cos(2\gamma)\sin\chi\\
&\qquad+\sin(2\alpha)\sin(2\gamma)\sin\kappa\big)\Big]^2+\Big[4\cos\alpha\sin^2\gamma\sin(4\gamma)\cos\kappa-8\csc^2\alpha\cos\alpha\sin^4\gamma\sin(2\gamma)\\
&\qquad\cdot\cos(2\alpha)\cos\chi\Big]^2\Big\}\Big/\Big[\big(4\cos\alpha\sin^2\gamma\sin(4\gamma)\cos\kappa-8\csc^2\alpha\cos\alpha\sin^4\gamma\sin(2\gamma)\cos(2\alpha)\cos\chi\big)\\
&\qquad\cdot\big(16\csc\alpha\cos^2\alpha\sin^4\gamma\sin(2\gamma)\sin\chi+8\cos\alpha\sin^2\gamma\cos^2(2\gamma)\sin\kappa\big)+32\csc\alpha\cos\alpha\sin^2\gamma\\
&\qquad\cdot\cos(2\gamma)\sin^2\gamma\cos^2(2\gamma)\big(\cos(2\alpha)\cos(2\gamma)\sin\chi+\sin(2\alpha)\sin(2\gamma)\sin\kappa\big)\big(\cos\chi-\cos\kappa\big)\Big]^2,
\end{aligned}
\tag{A10}
$$

$$
\begin{aligned}
&C=-\frac{M_1N_1+M_2N_2}{\big(M_2N_1-M_1N_2\big)^2}\\
&\quad=\big[\sin\alpha+2\cos\alpha\sin(2\gamma)+\sin(\alpha-4\gamma)\big]^2\Big[4\csc\alpha\sin^2\gamma\cos(2\gamma)\big(\cos(2\alpha)\cos(2\gamma)\sin\chi+\sin(2\alpha)\sin(2\gamma)\sin\kappa\big)\\
&\qquad\cdot\big(16\csc\alpha\cos^2\alpha\sin^4\gamma\sin(2\gamma)\sin\chi+8\cos\alpha\sin^2\gamma\cos^2(2\gamma)\sin\kappa\big)-8\sin^2\gamma\cos\alpha\cos^2(2\gamma)\big(\cos\chi-\cos\kappa\big)\\
&\qquad\cdot\big(4\cos\alpha\sin^2\gamma\sin(4\gamma)\cos\kappa-8\csc^2\alpha\cos\alpha\sin^4\gamma\sin(2\gamma)\cos(2\alpha)\cos\chi\big)\Big]\Big/\Big[\big(4\cos\alpha\sin^2\gamma\sin(4\gamma)\cos\kappa\\
&\qquad-8\csc^2\alpha\cos\alpha\sin^4\gamma\sin(2\gamma)\cos(2\alpha)\cos\chi\big)\big(16\csc\alpha\cos^2\alpha\sin^4\gamma\sin(2\gamma)\sin\chi+8\cos\alpha\sin^2\gamma\cos^2(2\gamma)\sin\kappa\big)\\
&\qquad+32\csc\alpha\cos\alpha\sin^2\gamma\cos(2\gamma)\sin^2\gamma\cos^2(2\gamma)\big(\cos(2\alpha)\cos(2\gamma)\sin\chi+\sin(2\alpha)\sin(2\gamma)\sin\kappa\big)\big(\cos\chi-\cos\kappa\big)\Big]^2.
\end{aligned}
\tag{A11}
$$

Substituting Eqs. (A9)–(A11) into Eqs. (A4)– (A7), analytical expressions for the characteristic parameters of any oblique elliptic stress path can be derived as follows:

$$\begin{aligned}\sin(2\theta)&=\frac{2C}{-\sqrt{(A-B)^2+4C^2}}\\&=-2\Big[16\sin\alpha\sin(2\alpha)\cos(2\gamma)\big(\cos(2\alpha)\cos(2\gamma)\sin\chi+\sin(2\alpha)\sin(2\gamma)\sin\kappa\big)\big(2\cos\alpha\sin(2\gamma)\sin^2\gamma\\&\cdot\sin\chi+\cos^2(2\gamma)\sin\alpha\sin\kappa\big)-32\cos\alpha\sin\alpha\sin(2\alpha)\sin(2\gamma)\cos^2(2\gamma)\big(\sin^2\alpha\cos(2\gamma)\cos\kappa\\&-\sin^2\gamma\cos(2\alpha)\cos\chi\big)\big(\cos\chi-\cos\kappa\big)\Big]\Big/\Big\{\Big\{\Big[4\sin(2\alpha)\big(2\cos\alpha\sin(2\gamma)\sin^2\gamma\sin\chi+\cos^2(2\gamma)\\&\cdot\sin\alpha\sin\kappa\big)\Big]^2+\Big[4\sin\alpha\sin(2\alpha)\cos^2(2\gamma)\big(\cos\chi-\cos\kappa\big)\Big]^2-\Big[4\sin\alpha\cos(2\gamma)\big(\cos(2\alpha)\cos(2\gamma)\sin\chi\\&+\sin(2\alpha)\sin(2\gamma)\sin\kappa\big)\Big]^2-\Big[8\cos\alpha\sin(2\gamma)\big(\sin^2\alpha\cos(2\gamma)\cos\kappa-\sin^2\gamma\cos(2\alpha)\cos\chi\big)\Big]^2\Big\}^2\\&+4\Big[-16\sin\alpha\sin(2\alpha)\cos(2\gamma)\big(\cos(2\alpha)\cos(2\gamma)\sin\chi+\sin(2\alpha)\sin(2\gamma)\sin\kappa\big)\big(2\cos\alpha\sin(2\gamma)\sin^2\gamma\\&\cdot\sin\chi+\cos^2(2\gamma)\sin\alpha\sin\kappa\big)+32\cos\alpha\sin\alpha\sin(2\alpha)\sin(2\gamma)\cos^2(2\gamma)\big(\sin^2\alpha\cos(2\gamma)\cos\kappa-\sin^2\gamma\\&\cdot\cos(2\alpha)\cos\chi\big(\cos\chi-\cos\kappa\big)\Big]^2\Big\}^{1/2},\end{aligned}\tag{A12a}$$

$$\begin{aligned}\cos(2\theta)&=\frac{A-B}{-\sqrt{(A-B)^2+4C^2}}\\&=-\Big\{\Big[4\sin(2\alpha)\big(2\cos\alpha\sin(2\gamma)\sin^2\gamma\sin\chi+\cos^2(2\gamma)\sin\alpha\sin\kappa\big)\Big]^2+\Big[4\sin\alpha\sin(2\alpha)\cos^2(2\gamma)\\&\cdot\big(\cos\chi-\cos\kappa\big)\Big]^2-\Big[4\sin\alpha\cos(2\gamma)\big(\cos(2\alpha)\cos(2\gamma)\sin\chi+\sin(2\alpha)\sin(2\gamma)\sin\kappa\big)\Big]^2-\big[8\cos\alpha\\&\cdot\sin(2\gamma)\big(\sin^2\alpha\cos(2\gamma)\cos\kappa-\sin^2\gamma\cos(2\alpha)\cos\chi\big)\Big]^2\Big\}\Big/\Big\{\Big\{\Big[4\sin(2\alpha)\big(2\cos\alpha\sin(2\gamma)\sin^2\gamma\sin\chi\\&+\cos^2(2\gamma)\sin\alpha\sin\kappa\big)\Big]^2+\Big[4\sin\alpha\sin(2\alpha)\cos^2(2\gamma)\big(\cos\chi-\cos\kappa\big)\Big]^2-\Big[4\sin\alpha\cos(2\gamma)\big(\cos(2\alpha)\\&\cdot\cos(2\gamma)\sin\chi+\sin(2\alpha)\sin(2\gamma)\sin\kappa\big)\Big]^2-\Big[8\cos\alpha\sin(2\gamma)\big(\sin^2\alpha\cos(2\gamma)\cos\kappa-\sin^2\gamma\cos(2\alpha)\\&\cdot\cos\chi\big)\Big]^2\Big\}^2+4\Big[-16\sin\alpha\sin(2\alpha)\cos(2\gamma)\big(\cos(2\alpha)\cos(2\gamma)\sin\chi+\sin(2\alpha)\sin(2\gamma)\sin\kappa\big)\\&\cdot\big(2\cos\alpha\sin(2\gamma)\sin^2\gamma\sin\chi+\cos^2(2\gamma)\sin\alpha\sin\kappa\big)+32\cos\alpha\sin\alpha\sin(2\alpha)\sin(2\gamma)\cos^2(2\gamma)\\&\cdot\big(\sin^2\alpha\cos(2\gamma)\cos\kappa-\sin^2\gamma\cos(2\alpha)\cos\chi\big)\big(\cos\chi-\cos\kappa\big)\Big]^2\Big\}^{1/2},\end{aligned}\tag{A12b}$$

$$\begin{aligned}\delta^2&=\frac{L_{\mathrm{b}}^2}{L_{\mathrm{a}}^2}=\frac{A+B-\sqrt{(A-B)^2+4C^2}}{A+B+\sqrt{(A-B)^2+4C^2}}\\&=\Big\{\Big[4\sin(2\alpha)\big(2\cos\alpha\sin(2\gamma)\sin^2\gamma\sin\chi+\cos^2(2\gamma)\sin\alpha\sin\kappa\big)\Big]^2+\Big[4\sin\alpha\sin(2\alpha)\cos^2(2\gamma)\\&\cdot\big(\cos\chi-\cos\kappa\big)\Big]^2+\Big[4\sin\alpha\cos(2\gamma)\big(\cos(2\alpha)\cos(2\gamma)\sin\chi+\sin(2\alpha)\sin(2\gamma)\sin\kappa\big)\Big]^2\\&+[8\cos\alpha\sin(2\gamma)\big(\sin^2\alpha\cos(2\gamma)\cos\kappa-\sin^2\gamma\cos(2\alpha)\cos\chi\big)\Big]^2-\Big\{\Big\{\Big[4\sin(2\alpha)\big(2\cos\alpha\sin(2\gamma)\\&\cdot\sin^2\gamma\sin\chi+\cos^2(2\gamma)\sin\alpha\sin\kappa\big)\Big]^2+\Big[4\sin\alpha\sin(2\alpha)\cos^2(2\gamma)\big(\cos\chi-\cos\kappa\big)\Big]^2-\big[4\sin\alpha\end{aligned}$$

$$\cdot\cos(2\gamma)\left(\cos(2\alpha)\cos(2\gamma)\sin\chi+\sin(2\alpha)\sin(2\gamma)\sin\kappa\right)\Big]^2-\Big[8\cos\alpha\sin(2\gamma)\left(\sin^2\alpha\cos(2\gamma)\cos\kappa\right.$$
$$\left.-\sin^2\gamma\cos(2\alpha)\cos\chi\right)\Big]^2\Big\}^2+4\Big[-16\sin\alpha\sin(2\alpha)\cos(2\gamma)\left(\cos(2\alpha)\cos(2\gamma)\sin\chi+\sin(2\alpha)\right.$$
$$\cdot\sin(2\gamma)\sin\kappa\left)\left(2\cos\alpha\sin(2\gamma)\sin^2\gamma\sin\chi+\cos^2(2\gamma)\sin\alpha\sin\kappa\right)+32\cos\alpha\sin\alpha\sin(2\alpha)\right.$$
$$\left.\cdot\sin(2\gamma)\cos^2(2\gamma)\left(\sin^2\alpha\cos(2\gamma)\cos\kappa-\sin^2\gamma\cos(2\alpha)\cos\chi\right)\left(\cos\chi-\cos\kappa\right)\Big]^2\Big\}^{1/2}\right\}$$
$$\Big/\Big\{\Big[4\sin(2\alpha)\left(2\cos\alpha\sin(2\gamma)\sin^2\gamma\sin\chi+\cos^2(2\gamma)\sin\alpha\sin\kappa\right)\Big]^2+\Big[4\sin\alpha\sin(2\alpha)\cos^2(2\gamma)$$
$$\cdot\left(\cos\chi-\cos\kappa\right)\Big]^2+\Big[4\sin\alpha\cos(2\gamma)\left(\cos(2\alpha)\cos(2\gamma)\sin\chi+\sin(2\alpha)\sin(2\gamma)\sin\kappa\right)\Big]^2+\Big[8\cos\alpha$$
$$\cdot\sin(2\gamma)\left(\sin^2\alpha\cos(2\gamma)\cos\kappa-\sin^2\gamma\cos(2\alpha)\cos\chi\right)\Big]^2+\Big\{\Big\{\Big[4\sin(2\alpha)\left(2\cos\alpha\sin(2\gamma)\sin^2\gamma\sin\chi\right.$$
$$\left.+\cos^2(2\gamma)\sin\alpha\sin\kappa\right)\Big]^2+\Big[4\sin\alpha\sin(2\alpha)\cos^2(2\gamma)\left(\cos\chi-\cos\kappa\right)\Big]^2-\Big[4\sin\alpha\cos(2\gamma)\left(\cos(2\alpha)\right.$$
$$\left.\cdot\cos(2\gamma)\sin\chi+\sin(2\alpha)\sin(2\gamma)\sin\kappa\right)\Big]^2-\Big[8\cos\alpha\sin(2\gamma)\left(\sin^2\alpha\cos(2\gamma)\cos\kappa-\sin^2\gamma\cos(2\alpha)\right.$$
$$\left.\cdot\cos\chi\right)\Big]^2\Big\}^2+4\Big[-16\sin\alpha\sin(2\alpha)\cos(2\gamma)\left(\cos(2\alpha)\cos(2\gamma)\sin\chi+\sin(2\alpha)\sin(2\gamma)\sin\kappa\right)$$
$$\cdot\left(2\cos\alpha\sin(2\gamma)\sin^2\gamma\sin\chi+\cos^2(2\gamma)\sin\alpha\sin\kappa\right)+32\cos\alpha\sin\alpha\sin(2\alpha)\sin(2\gamma)\cos^2(2\gamma)$$
$$\left.\cdot\left(\sin^2\alpha\cos(2\gamma)\cos\kappa-\sin^2\gamma\cos(2\alpha)\cos\chi\right)\left(\cos\chi-\cos\kappa\right)\Big]^2\Big\}^{1/2}\right\}, \tag{A13}$$

$$L_{\mathrm{a}}^2=\frac{2}{A+B-\sqrt{(A-B)^2+4C^2}}$$
$$=2\sin^2\gamma\csc^2\alpha\Big[32\cos\alpha\sin(2\alpha)\sin(2\gamma)\left(\sin^2\alpha\cos(2\gamma)\cos\kappa-\sin^2\gamma\cos(2\alpha)\cos\chi\right)\left(2\cos\alpha\sin(2\gamma)\right.$$
$$\left.\cdot\sin^2\gamma\sin\chi+\cos^2(2\gamma)\sin\alpha\sin\kappa\right)+16\sin^2\alpha\sin(2\alpha)\cos(2\gamma)\cos^2(2\gamma)\left(\cos(2\alpha)\cos(2\gamma)\sin\chi\right.$$
$$\left.+\sin(2\alpha)\sin(2\gamma)\sin\kappa\right)\left(\cos\chi-\cos\kappa\right)\Big]^2\Big/\Big\{\Big\{\Big[4\sin(2\alpha)\left(2\cos\alpha\sin(2\gamma)\sin^2\gamma\sin\chi+\cos^2(2\gamma)\sin\alpha\right.$$
$$\left.\cdot\sin\kappa\right)\Big]^2+\Big[4\sin\alpha\sin(2\alpha)\cos^2(2\gamma)\left(\cos\chi-\cos\kappa\right)\Big]^2+\Big[4\sin\alpha\cos(2\gamma)\left(\cos(2\alpha)\cos(2\gamma)\sin\chi\right.$$
$$\left.+\sin(2\alpha)\sin(2\gamma)\sin\kappa\right)\Big]^2+\Big[8\cos\alpha\sin(2\gamma)\left(\sin^2\alpha\cos(2\gamma)\cos\kappa-\sin^2\gamma\cos(2\alpha)\cos\chi\right)\Big]^2$$
$$-\Big\{\Big\{\Big[4\sin(2\alpha)\left(2\cos\alpha\sin(2\gamma)\sin^2\gamma\sin\chi+\cos^2(2\gamma)\sin\alpha\sin\kappa\right)\Big]^2+\Big[4\sin\alpha\sin(2\alpha)\cos^2(2\gamma)$$
$$\cdot\left(\cos\chi-\cos\kappa\right)\Big]^2-\Big[4\sin\alpha\cos(2\gamma)\left(\cos(2\alpha)\cos(2\gamma)\sin\chi+\sin(2\alpha)\sin(2\gamma)\sin\kappa\right)\Big]^2-\Big[8\cos\alpha\sin(2\gamma)$$
$$\cdot\left(\sin^2\alpha\cos(2\gamma)\cos\kappa-\sin^2\gamma\cos(2\alpha)\cos\chi\right)\Big]^2\Big\}^2+4\Big[-16\sin\alpha\sin(2\alpha)\cos(2\gamma)\left(\cos(2\alpha)\cos(2\gamma)\sin\chi\right.$$
$$\left.+\sin(2\alpha)\sin(2\gamma)\sin\kappa\right)\left(2\cos\alpha\sin(2\gamma)\sin^2\gamma\sin\chi+\cos^2(2\gamma)\sin\alpha\sin\kappa\right)+32\cos\alpha\sin\alpha\sin(2\alpha)$$
$$\left.\cdot\sin(2\gamma)\cos^2(2\gamma)\left(\sin^2\alpha\cos(2\gamma)\cos\kappa-\sin^2\gamma\cos(2\alpha)\cos\chi\right)\left(\cos\chi-\cos\kappa\right)\Big]^2\Big\}^{1/2}\right\}$$
$$\cdot\left[\sin\alpha+2\cos\alpha\sin(2\gamma)+\sin(\alpha-4\gamma)\right]^2\Big\}. \tag{A14}$$

中文概要

题　目： P 波斜入射形成的动应力路径及影响因素分析

目　的： 研究 P 波斜入射下的地基动应力路径，探讨其影响因素和可能变化范围，为进一步研究斜入射地震波作用下场地动力响应奠定理论基础。

创新点： 1. 从数学上证明斜入射 P 波在任一深度的地基中形成的应力路径在剪应力分量（偏差正应力-水平剪应力）组成的平面中为一个斜椭圆；2. 分析了 P 波入射角、土体泊松比和单位波长深度对斜椭圆应力路径形状与大小的影响。

方　法： 1. 基于半无限弹性空间的地震波传播理论，考虑地震波在自由界面的反射，推导土体中任一深度处由 P 波斜入射产生的动应力，并表示成由剪应力分量组成的平面下的应力路径（公式（9））及该应力路径的特征参数表达式（公式（A12）～（A14））；2. 通过控制变量法，分析参数敏感性（图 7、9、10 和 12）。

结　论： 1. 虽然证实 P 波斜入射引起的应力路径为斜椭圆形式，但在地基深度、入射波频率和波速的特定组合下，斜椭圆仍可从斜线一直变化到圆形，形式较为多样化；2. P 波斜入射角度在 30°~60° 时引起的动偏应力幅最大，最大可达同等条件下其它入射角产生的动应力幅的 2 倍以上；3. 斜入射角大于 45°后，斜椭圆路径形状几乎不随入射角改变，在研究范围内以竖直扁椭圆形为主；4. 土体饱和度大于 70%时，泊松比的变化对土体斜椭圆路径形状影响不大，但动应力幅随泊松比增大而显著降低。

关键词： 近场地震；P 波；斜入射；弹性半空间；动应力路径